Inorganic Chemistry

Article

pubs.acs.org/IC

Theoretical Predictions of Novel Superconducting Phases of $BaGe_3$ Stable at Atmospheric and High Pressures

Eva Zurek*[,†] and Yansun Yao*[,‡,¶]

[†]Department of Chemistry, State University of New York at Buffalo, Buffalo, New York 14260-3000, United States
[‡]Department of Physics and Engineering Physics, University of Saskatchewan, Saskatoon, Saskatchewan S7N 5E2, Canada
[¶]Canadian Light Source, Saskatoon, Saskatchewan S7N 0X4, Canada

Supporting Information

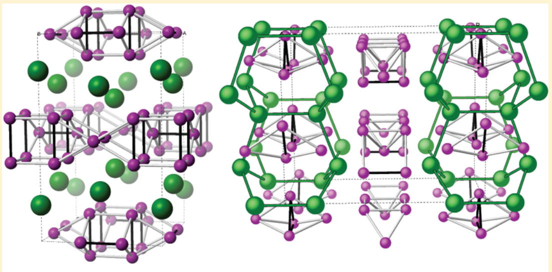

I4/mmm-$BaGe_3$, T_c = 5.5 K   *Amm2*-$BaGe_3$, T_c = 4.5 K

ABSTRACT: A series of new superconducting binary silicides and germanides have recently been synthesized under high-pressure high-temperature conditions. A representative member of this group, $BaGe_3$, was theoretically investigated using evolutionary structure searches coupled with structural analogies in the pressure range from 1 atm to 250 GPa, where three new phases were discovered. At 1 atm, in addition to the synthesized $P6_3/mmc$ phase, we predicted two new phases, $I4/mmm$ and $Amm2$, to be dynamically stable. The $Amm2$ structure comprises Ge clusters and triangular prisms intercalated with Ba and Ge atoms, a unique structural motif unknown to this group. The $I4/mmm$ structure has been previously synthesized in binary silicides and is calculated to be thermodynamically stable in $BaGe_3$ between 15.6 and 35.4 GPa. Above 35.4 GPa, two new phases of $P\bar{6}m2$ and $R\bar{3}m$ symmetry become the global minima and remain so up to the highest pressure considered. These two phases have very similar enthalpies, and both feature layers of double Kagome nets of Ge intercalated with Ba−Ge layers. The predicted phases are suggested to be metallic with itinerant electrons and to be potentially superconducting from the considerable electron−phonon coupling strength. Density functional perturbation calculations combined with the Allen−Dynes-modified McMillan formula were used to estimate the superconducting critical temperatures (T_c) for these new phases, which, with slight pressure variations, are comparable to the experimental T_c measured for the $P6_3/mmc$ phase.

■ INTRODUCTION

The pressure-induced structural transitions of elemental germanium have been studied intensely. The semiconducting diamond form transforms to a metallic β-Sn phase (space group $I4_1/amd$) at 10 GPa,[1] and upon increasing pressure the following transitions are observed: $Imma \rightarrow P6/mmm$ (*sh*) $\rightarrow$ $Cmca$ → hcp at 75, 85, 100, and 170 GPa,[2−4] respectively. Superconductivity at 11.5 GPa was found below 5.35 K.[5] Importantly, unique metastable structures of this tetrel element are accessible at or near ambient conditions. For example, chemical techniques have been employed to synthesize a beautiful Type-II clathrate structure,[6] and controlled pressure release led to the formation of metastable phases, which were shown to become superconducting below 3 GPa.[7] Upon reducing or quenching the β-Sn phase to atmospheric pressure, various metastable phases of germanium are obtained, depending on the depressurization rate. By slowly unloading the pressure, a semiconducting ST12 phase (space group $P4_32_12$) has been observed.[8] Upon a rapid pressure release, a BC8 structure (space group $Ia\bar{3}$) was found.[9] Very recently, evidence for the formation of an R8 phase (space group $R\bar{3}$) on pressure release was also found in germanium through an experimental study using indentation techniques.[10] In addition, a "host−guest" germanium allotrope has been synthesized under pressure.[11] Other metastable phases, one of which has been calculated as being superconducting below ∼9 K at 1 atm,[12] have recently been predicted computationally using the metadynamics technique. Elemental germanium is believed to behave as a standard BCS-type superconductor, and the electron−phonon coupling parameter, λ, as well as the temperature below which superconductivity is predicted to occur (within the modified Allen−Dynes formalism), T_c, has been calculated to increase with decreasing pressure for various phases.[12,13]

Yet, the spectrum of structures this tetrel element can adopt is even more extensive upon formation of polar intermetallic compounds. Some examples of common motifs include one-dimensional ${}^{1}_{\infty}[Ge_2]$ chains in either the zigzag[14] or *cis*−*trans*[14] configurations, two-dimensional (2D) three-connected nets (for example, a puckered variant of the AlB_2 structure[15]), and three-dimensional configurations such as the connected net characteristic of α-$ThSi_2$,[16] or four-coordinate cagelike structures.[17] Zero-dimensional motifs including a *trans*-butene-like $[Ge_4]$ anionic fragment,[18] dimers[19] (which sometimes condense into 2D arrays ${}^{2}_{\infty}[Ge_2]^{20}$) or polyhedral homoatomic clusters[21] including the tetrahedral $[Ge_4]^{4-}$, the butterfly $[Ge_4]^{6-}$ and the pyramidal $[Ge_5]^{x-}$ clusters represent only a few of the motifs[22] that are known. Relevant for this work are the (nearly)

Received: December 18, 2014
Published: March 2, 2015

DOI: 10.1021/ic5030235
Inorg. Chem. 2015, 54, 2875−2884

tetragonal pyramidal Ge_5^{6-} and Ge_5^{4-} clusters present in Eu_3Ge_5[23] and Yb_3Ge_5,[24] whose structures are isotypic with Sr_3Sn_5, Ba_3Sn_5, and Ba_3Pb_5.[25,26]

The amazing diversity in the polar intermetallics originates from their inherent ability (and flexibility) to adopt different bonding strategies. On the one hand, the Zintl concept[27] can be employed to explain the crystal and electronic structures of *sp*-bonded salt-like compounds that are typically semiconducting. However, many polar intermetallics do not adhere to these electron-precise counting schemes and exhibit delocalized metallic bonding.[28] The formation of unusually high coordination environments, which can be accomplished using high-pressure synthesis techniques, is one way to experimentally access metallic phases.

Indeed, analogous to elemental germanium, high-pressure (and temperature) synthesis has expanded the range of stoichiometries and structures that can be quenched to atmospheric conditions. Coordination numbers as high as eight have been obtained, the latter in a set of lanthanum pentagermanides.[29,30] Recently, a $BeGe_6$ phase where the germanium lattice consists of tubular voids filled with Ba atoms,[31] and a $BeGe_5$ phase containing 2D germanium slabs separated by layers of barium[32] have been synthesized at high pressures and temperatures. Consider, moreover, the $P6_3/mmc$-$BaGe_3$ phase, which is comprised of columns of face-sharing elongated Ge_6 octahedra.[33] Or the $LaGe_3$ structure, which crystallizes in the space group $R\bar{3}m$ and contains triangular Ge_3 units.[34] Another example is an $I4/mmm$-$CaGe_3$ structure, whose constituents include Ge_2 dimers that condense to form square prisms that are capped on either side by another set of Ge_2 dimers.[35] This unique structure was further observed in the binary silicides $CaSi_3$, YSi_3, and $LuSi_3$.[36] All of the aforementioned MGe_3 phases were shown to be superconducting with T_c values ranging from 4 K to 7.4 K. First-principles calculations indicate that they behave as BCS-type phonon mediated superconductors.[35,36]

The pressures employed in these experiments have typically been below 15 GPa. This made us wonder if the application of higher pressures could lead to the formation of hitherto unknown phases, which could be quenched to atmospheric conditions. How could we understand their electronic structures, and could electricity pass through them without resistance? The rich structural diversity of germanium-containing polar intermetallics hints that there are many new phases, perhaps with unique properties, awaiting to be discovered. In this contribution we focus on the $BaGe_3$ stoichiometry. Structural analogies and evolutionary algorithms[37] are coupled with first-principles calculations to predict three new stable metallic phases under pressure, two of which are metastable at 1 atm. The bonding within them, and their electronic structure, is interrogated. The temperatures at which these phases become superconducting are calculated as a function of pressure. Structures with $Amm2$ and $I4/mmm$ symmetry are predicted to have a T_c slightly higher than the recently synthesized $P6_3/mmc$-$BaGe_3$.[33]

■ RESULTS AND DISCUSSION

Structural Diversity in the Germanium Lattices: From Edge-Sharing Octahedra to Double Kagome Lattices. To uncover the structures of the thermodynamically stable $BaGe_3$ phases under pressure, structure searches were performed using the open-source evolutionary algorithm (EA) XtalOpt. Calculations were also carried out on a $BaGe_3$ configuration with $I4/mmm$ symmetry isotypic with the recently synthesized $CaGe_3$, $CaSi_3$, YSi_3, and $LuSi_3$ phases.[35,36] Up to pressures of 250 GPa, the formation of the binary germanide from the elemental solids was calculated to be thermodynamically favorable. Figure 1 traces out the relative enthalpies of the important phases found in this study, whereas Table 1 lists the calculated ranges of stability for these structures and their previous precedents in Group IV binaries.

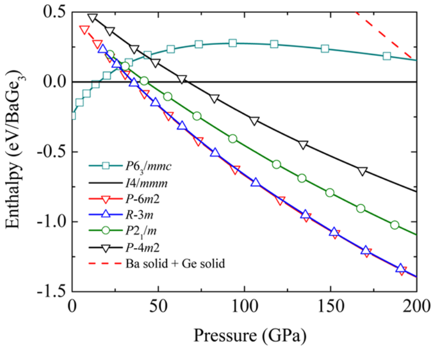

Figure 1. Enthalpies of select $BaGe_3$ phases found in our evolutionary searches, relative to the enthalpy of the $I4/mmm$ symmetry structure. For solid barium, the structure sequence bcc → hcp→ $I4/mcm$→ hcp was used for the enthalpy calculations.[38] For solid germanium, the structure sequence diamond → β-tin→ $Imma$ → simple hexagonal → hcp was used.[39]

Table 1. Calculated Ranges of Stability for the Candidate Structures of $BaGe_3$[a]

structure	range of stability	isostructural binaries
$P6_3/mmc$	0.0−15.6 GPa	$BaGe_3$,[33] $BaSn_3$[40]
$I4/mmm$	15.6−35.4 GPa	$CaGe_3$,[35] $CaSi_3$,[36] YSi_3,[36] $LuSi_3$[36]
$P\bar{6}m2$	>35.4 GPa	theoretical prediction[b]
$R\bar{3}m$	>35.4 GPa	theoretical prediction[b]

[a] Group IV binaries that are isostructural to the $P6_3/mmc$ and $I4/mmm$ structures are listed. [b] The phrase "theoretical predication" indicates that the structure has yet to be synthesized.

At 0 GPa, the most stable structure unearthed by evolutionary structure searches had $P6_3/mmc$ symmetry, and its primitive cell consisted of two $BaGe_3$ units. The EA search carried out at 25 GPa located two structures whose enthalpies were within 21 meV/atom of each other. The lower enthalpy system turned out to be the same $P6_3/mmc$ phase obtained in our ambient pressure searches. A slightly distorted version of this structure, with $P2_1/m$ symmetry, was also unearthed. The EA did not find the $I4/mmm$ structure, which is assumed by a number of binary silicides and germanides, whose enthalpy turned out to be 21 meV/atom lower than that of the $P6_3/mmc$ configuration. This difference in enthalpy is comparable to the energy difference between diamond and graphite at 1 atm. The fact that the EA correctly identified the $P6_3/mmc$ structure at 1 atm, but did not find $I4/mmm$-$BaGe_3$ at 25 GPa is not necessarily surprising. There is perhaps no guarantee that any of the structure prediction methods commonly used nowadays[41] will find the global minimum of a given potential energy surface (PES) unless the method visits every local minima. Moreover, since many of these methods are stochastic in nature (meaning that, for a given stoichimetry, each individual search may explore different regions of the PES, even if the same search criteria are used) one may need to carry out numerous searches to find the global minimum. Since structural analogies were able to show that the $I4/mmm$ phase was stable within the pressure range of 25−50 GPa, it was not necessary to carry out further computationally demanding EA searches at these pressures.

Evolutionary searches carried out at 50, 150, and 250 GPa located two distinct, isoenthalpic structures with four formula units in the primitive cell. One of these had $R\bar{3}m$ (space group No. 166) symmetry, whereas the other one was of $P\bar{6}m2$ (space group No. 187) symmetry. Within this pressure range, the molar volumes of these two phases were nearly identical, and if the EA had identified duplicate structures based on a "fingerprint" consisting of their enthalpies and volumes, followed by subsequent removal of one set of duplicates from the gene pool, it is likely that only one of these phases would have been found in the structure search. This highlights the importance of using a niching scheme that performs an exact (to within a specified tolerance), rather than an approximate comparison of two structures, as is done via the XtalComp algorithm[42] that is embedded within XtalOpt. For pressures above 50 GPa, the $R\bar{3}m$ and $P\bar{6}m2$ $BaGe_3$ phases were significantly more stable than any others that we encountered. For example, at 50 GPa, the enthalpies of the second and third most stable structures were 40 meV/atom and 78 meV/atom higher, respectively. The former corresponds to the previously mentioned $P2_1/m$ symmetry structure, which contained four formula units in the primitive cell, whereas the latter configuration had $P\bar{4}m2$ symmetry with three formula units. These two phases were also located in evolutionary runs performed at 150 and 250 GPa. At 250 GPa, the $P2_1/m$ phase maintained its rank as the second most stable structure, separated by a 90 meV/atom window from the reigning global minima, $R\bar{3}m$ and $P\bar{6}m2$ $BaGe_3$.

The $P6_3/mmc$ structure, which was predicted to be the most stable at pressures <15.6 GPa, is identical to the binary germanide that was recently synthesized at high temperatures and pressures ranging from 3 GPa to 13 GPa,[33] and is isotypic to the $BaSn_3$ structure.[40] It consists of layers of Ge_3 equilateral triangles whose edges measure 2.676 Å in our calculations (cf. 2.613(4) Å in experiment) and Ba atoms. Examining the structure down the *c*-axis, the Ba atoms become superimposed, whereas the Ge_3 triangles twist by 60° from layer to layer. The distance between Ge atoms in the two sets of layers, 2.917 Å, compares well with the distance determined experimentally (2.932 Å). If one considers these elongated Ge−Ge contacts to possess a bonding interaction, then the structure can be thought of as containing one-dimensional chains of elongated edge-sharing Ge_6 octahedra, as illustrated in Figure 2a. The lattice vectors we calculate, $a = 6.929$ Å and $c = 4.950$ Å, differ by <2% from those determined experimentally ($a = 6.814$ Å and $c = 5.027$ Å).

An $I4/mmm$ phase isotypic with a $CaGe_3$ structure[35] that was recently synthesized at 10 GPa was calculated as having the lowest enthalpy within a narrow pressure range of 15.6−35.4 GPa (see Figure 2b). In agreement with our results, prior theoretical studies have found that a $CaSi_3$ structure can only be synthesized in a slim pressure range.[43] The germanium sublattice in the $I4/mmm$ phases consists of Ge_2 dumbbells with short Ge−Ge bonds running parallel to the *c*-axis. Longer Ge−Ge contacts link adjacent dimers so that they form square prisms, which are capped by a further set of Ge_2 dumbbells in two perpendicular orientations. This unique bonding pattern gives rise to a 2D lattice of condensed Ge_2 dimers where each Ge atom adopts (1 + 4) homonuclear contacts. Another way to describe the germanium lattice is as edge-sharing triangular prisms, where the shorter Ge−Ge bonds correspond to the shared vertices. The calculated short (long) Ge−Ge bonds in $BaGe_3$ at 1 atm, 2.542 and 2.572 Å (2.845 and 2.846 Å), match up quite well with those observed experimentally in $CaGe_3$, 2.549 and 2.599 Å (2.763 and 2.823 Å). As expected, both the *a* and *c* lattice vectors are longer for $BaGe_3$ than $CaGe_3$ (7.915 and 12.935 Å, compared to 7.692 and 11.331 Å), because the structure needs to accommodate a larger alkaline-earth metal.

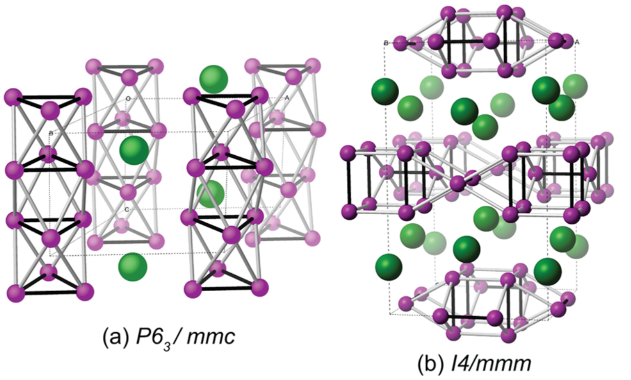
(a) $P6_3/mmc$

(b) $I4/mmm$

Figure 2. $BaGe_3$ structures of (a) $P6_3/mmc$ and (b) $I4/mmm$ symmetry. Black Ge−Ge contacts denote short bonds, whereas gray ones signify longer ones. Ba atoms are colored in green and Ge atoms in purple. Supercells are illustrated using a faint dashed line. $P6_3/mmc$-$BaGe_3$ has previously been synthesized.[33] Our calculations predict that $I4/mmm$-$BaGe_3$ will be a stable phase. $CaGe_3$, $CaSi_3$, YSi_3, and $LuSi_3$, with $I4/mmm$ symmetry, have previously been synthesized.[35,36]

The $R\bar{3}m$ and $P\bar{6}m2$ phases (see Figures 3a and 3b), calculated as being the most stable at pressures greater than ∼35.4 GPa, are related and their Ge lattice contains a unique structural motif. Ge_2 dumbbells condense to form two sets of 2D Kagome lattices, where each atom from the dimer comprises only one of these nets as illustrated in Figure 3c. At 40 GPa, the short and long Ge−Ge bonds measure 2.414−2.436 and 2.596−2.608 Å, and each atom has (1 + 4) homonuclear bonds. Actually, another way to view this lattice is a 2D arrangement of edge-sharing triangular prisms. In analogy with the $I4/mmm$ system, the shared edges assume shorter Ge−Ge distances. In addition, another Ge atom lies in the center of the hexagonal prisms comprising the double Kagome motif (at the 1f site), and it is located at a distance of 2.870−2.874 Å from 12 Ge atoms. At this pressure (i.e., 40 GPa), germanium adopts a β-Sn structure, and the two closest Ge−Ge contacts measure 2.46 and 2.57 Å.

In $R\bar{3}m$ and $P\bar{6}m2$ $BaGe_3$, layers of these 2D Ge networks are buffered by layers comprised of both the electropositive element and the tetrel. Interestingly, the Ba/Ge layers in the $R\bar{3}m$ and $P\bar{6}m2$ structures (Figures 3a and 3b, respectively) are isostructural to the slabs of the Laves phase structures $MgCu_2$ (C15) and $MgZn_2$ (C14). The Ba atoms assume an almost-diamondoid lattice, where each angle lies close to the one found in an ideal tetrahedron (109.08°−109.8°). The Ba−Ba contact that runs parallel to the *c*-axis is somewhat longer (3.397−3.416 Å) than the other two (3.184−3.202 Å). At 40 GPa, elemental barium adopts an hcp structure, within which the shortest Ba−Ba contacts connect the atoms in adjacent hexagonal layers (3.17 Å), and the contacts within the hexagonal layers are slightly longer (∼3.23 Å). The Ba−Ba distances within the $R\bar{3}m$ and $P\bar{6}m2$ phases of $BaGe_3$ are comparable to those in pure barium. This is consistent with the phase segregation found in the $BaGe_3$ structures, where the Ba phase carries some similarities to pure barium. The 2D Ba diamondoid lattice encompasses

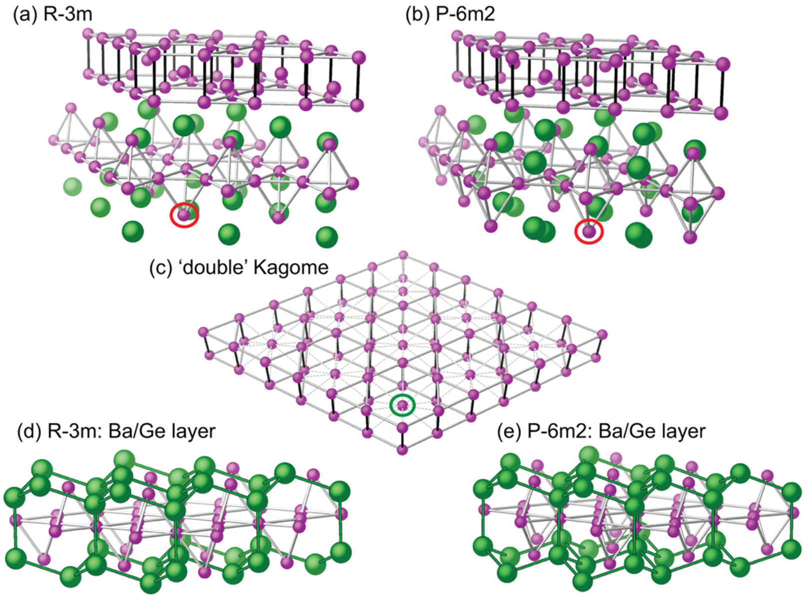

Figure 3. (a) $R\bar{3}m$ and (b) $P\bar{6}m2$ structures are composed of (c) "double Kagome" layers, as well as the Ba/Ge layers illustrated in panels (d) and (e), respectively. Black Ge–Ge contacts signify short bonds within Ge_2 dumbbells, whereas light gray and dotted lines correspond to progressively longer Ge–Ge distances. The two Ba/Ge layers differ by the placement of the Ge atom circled in red in panels (a) and (b). One of the Ge atoms that is located in the middle of a hexagonal prism constructed from the fusion of two Kagome lattices is emphasized by a green circle in panel (c).

one consisting of Ge atoms, which differs slightly for the two structures. In the $P\bar{6}m2$ phase, Ge_5 clusters with D_{3h} symmetry constitute this layer. The cluster is an equilateral triangle with one atom above, and another below it, at equal spacing. Actually, the Ge–Ge distances within the cluster (2.625–2.652 Å) are somewhat longer than the shortest distance between them, which measures 2.592 Å. The $R\bar{3}m$ structure can be constructed by moving one set of Ge atoms that all lie in the same plane (circled in red in Figures 3a and 3b). In $P\bar{6}m2$, these atoms constitute the apex in the Ge_5 cluster, and moving them gives rise to corner-sharing Ge_4 clusters instead. The base of the four-atom cluster is an equilateral triangle whose Ge–Ge distances measure 2.599 Å, and the distance between each of these Ge atoms and the apex is 2.678 Å.

Phonon calculations verified that the $P6_3/mmc$ (1 atm, 2 and 10 GPa), $I4/mmm$ (1 atm, 25 GPa), $R\bar{3}m$ (35 GPa), and $P\bar{6}m2$ (100 GPa) structures are dynamically stable at the pressures given in the parentheses. The $P6_3/mmc$ and $I4/mmm$ symmetry phases remain dynamically stable at 1 atm, so they are potentially accessible via high-pressure synthesis techniques. Indeed, $P6_3/mmc$-$BaGe_3$ has already been synthesized in the pressure range of 3–13 GPa and temperatures varying between 500 °C and 1200 °C.[33] Neither $R\bar{3}m$ nor $P\bar{6}m2$ $BaGe_3$ remains dynamically stable at 1 atm. However, when the 40 GPa $P\bar{6}m2$ structure was relaxed to 1 atm, which allowed the lattice to change symmetry, it transformed to an *Amm*2 structure that was found to be dynamically stable at 1 atm. Thus, our calculations have predicted two new structures that could potentially be synthesized under high pressure and quenched to atmospheric conditions. At 1 atm, the $I4/mmm$ and the *Amm*2 structures are 0.065 and 0.535 eV/$BaGe_3$ less stable than the $P6_3/mmc$ structure, respectively.

*Amm*2-$BaGe_3$, illustrated in Figure 4, is a distorted version of the $P\bar{6}m2$ structure. One can obtain the primitive cell of the former from the latter via the matrix

$$\begin{bmatrix} 1 & 1 & 0 \\ 1 & -1 & 0 \\ 0 & 0 & 1 \end{bmatrix}$$

followed by a slight distortion of the lattice parameters from hexagonal symmetry. This distortion reduces the symmetry of the Ge_5 cluster from D_{3h} to C_{2v}, so that two of the Ge–Ge distances in the triangular motif are somewhat longer than the third (2.675 Å vs 2.677 Å). Moreover, the double Kagome lattice transforms to triangular prisms that are connected to each other in one dimension by the isolated Ge atom found at the 1f site in the $P\bar{6}m2$ configuration.

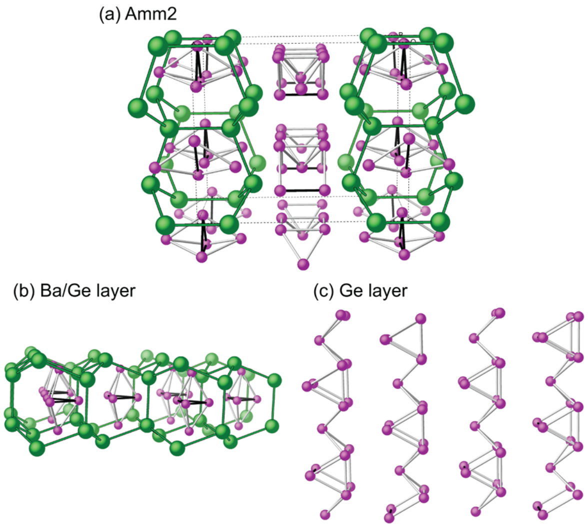

Figure 4. (a) Upon decompression to 1 atm, the $P\bar{6}m2$ $BaGe_3$ structure illustrated in Figure 3b transforms to the dynamically stable *Amm*2 phase, composed of layers containing (b) Ba and Ge atoms, as well as (c) Ge atoms.

Bonding at 1 atm. To gauge the strength of the Ge–Ge bonds in the $P6_3/mmc$ phase of $BaGe_3$, which is isotypic with the $BaSn_3$ structure,[40] the crystal orbital Hamilton populations (COHP) and the negative of the COHP integrated to the Fermi level (−ICOHP) were previously calculated.[33] The −ICOHP indicated that the bond within the triangular units was significantly stronger than the bond between them (2.1 vs 0.78 eV/bond mol). Features in the −ICOHP plot were rationalized by considering a schematic molecular orbital (MO) diagram that was previously proposed for $(Sn_3)^{2-}$ by Fässler et al.[40] (based on analogy with the isoelectronic, aromatic, cyclo-propanyl cations ($C_3R_3^+$)), and the bands that would form when these motifs condensed to a solid. The −ICOHPs that we calculate using the optimized geometry (see Table 2) are in good agreement with those obtained by Fukuoka and co-workers for the experimentally determined geometry. The bonding within the *I*4/*mmm* symmetry $CaSi_3$, YSi_3, $LuSi_3$ and $CaGe_3$ structures has also previously been studied.[35,36] The electron localizability indicator provided evidence for covalent two-center two-electron bonding between the Si atoms comprising the dumbbells, and multicenter interactions of Si/Ge with the Ca atoms. Since *I*4/*mmm*-$BaGe_3$ is isotypic with these structures, one would expect similar bonding characteristics. Indeed, we find the Ge(1)−Ge(1) and the short Ge(2)−Ge(2) contacts (see Figure 5a for the atom labeling) to have substantial −ICOHPs, comparable to those between Ge atoms comprising the equilateral triangles in the $P6_3/mmc$ phase. The strength of the Ge−Ge bonds measuring ~2.8 Å, on the other hand, was comparable to that between the Ge atoms belonging to two adjacent triangles in $P6_3/mmc$-$BaGe_3$.

Table 2. Select Ge−Ge Distances in the $BaGe_3$ Phases That Are Dynamically Stable at 1 atm, and Their Corresponding Crystal Orbital Hamiltonian Populations Integrated to the Fermi Level (−ICOHP)[a]

atom pair	distance (Å)	−ICOHP (eV/bond mol)
	P*6$_3$/*mmc	
Ge−Ge	2.676	1.83
Ge−Ge	2.917	0.80
	I*4/*mmm	
Ge(1)−Ge(1)	2.517	2.43
Ge(1)−Ge(2)	2.822	0.97
Ge(2)−Ge(2)	2.591	1.71
Ge(2)−Ge(2)	2.844	0.99
	***Amm*2**	
Ge(1)−Ge(1)	2.704	1.01
Ge(1)−Ge(1)	2.733	1.38
Ge(1)−Ge(2)	2.766	1.38
Ge(1)−Ge(3)	3.050	0.32
Ge(1)−Ge(6)	2.726	1.06
Ge(2)−Ge(2)	2.635	1.08
Ge(2)−Ge(3)	2.989	0.49
Ge(3)−Ge(4)	2.830	1.33
Ge(3)−Ge(5)	2.819	1.33
Ge(4)−Ge(4)	2.678	1.74
Ge(4)−Ge(5)	2.675	1.76

[a] The short and long Ge−Ge bonds in the $P6_3/mmc$ and *I*4/*mmm* structures are denoted by the black and white contacts illustrated in Figure 2, and select atom pairs are illustrated in Figure 5.

What are the important structural motifs within *Amm*2-$BaGe_3$? Are they Ge dumbbells, triangles, or perhaps the Ge_5 clusters that are encapsulated within a 2D barium lattice? To answer this question, the −ICOHPs and Ge−Ge bond lengths were compared to those found in the $P6_3/mmc$ and *I*4/*mmm* structures. Let us first consider the Ge atoms comprising the triangular prisms in the 2D Ge lattice. The Ge−Ge distances within a single triangle (2.733 and 2.766 Å) are <0.1 Å longer than those found within the equilateral triangles comprising the $P6_3/mmc$ phase. Accordingly, the −ICOHPs are also ~25% smaller, but they are still indicative of substantial bonding. Interestingly, even though the nearest-neighbor Ge−Ge distances between atoms belonging to two different triangles are shorter than those within a single triangle, the −ICOHPs between them are smaller. That is to say, the Ge(2)−Ge(2) bond measuring 2.635 Å is 22% weaker than the 2.766 Å Ge(1)−Ge(2) bond. This seemingly contradictory finding is consistent with the Electron Localization Function (ELF) plot illustrated in Figure 6.

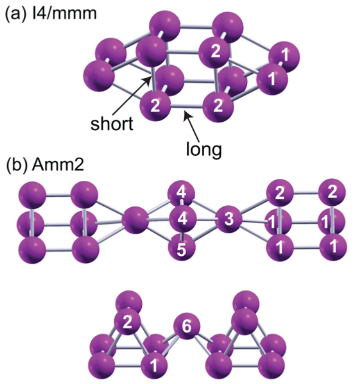

Figure 5. Symmetry-inequivalent Ge atoms found in $BaGe_3$ at 1 atm: (a) *I*4/*mmm* and (b) *Amm*2. In panel (a) (*I*4/*mmm* symmetry), for the sake of clarity, the Ge(1)−Ge(1) dumbbells capping the front and back face of the cube in *I*4/*mmm* $BaGe_3$ are not shown (see Figure 2b), and one of the short Ge(2)−Ge(2) contacts and one of the long Ge(2)−Ge(2) contacts is explicitly denoted. In panel (b) (*Amm*2), the top panel highlights the connectivity between the triangular prisms and Ge_5 clusters, whereas the bottom panel illustrates how the triangular prisms are connected. The full Ge lattice is shown in Figure 4.

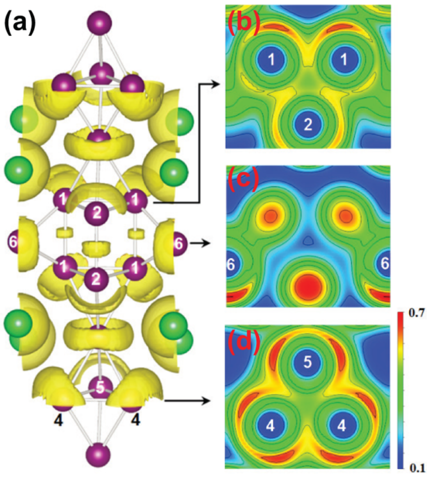

Figure 6. (a) An isosurface (ELF = 0.6) of the electron localization function shown in an irreducible region of the unit cell of the *Amm*2 structure at atmospheric pressure. (b−d) The ELF contour maps in different horizontal planes. The positions of the planes are marked by arrows.

As an intuitive approach for investigating the bonding in extended structures, the ELF is a measure of relative electron localization, with respect to a uniform electron gas of the same density. Large ELF values identify regions in the structure where there is a high tendency of electron pairing, such as cores, bonds, and lone pairs. The ELF contours mapped on a single triangle of Ge (Figure 6b) recovers neatly its bonding pattern; electrons clearly tend to pair between the Ge(1) and Ge(2) atoms, and between two Ge(1) atoms, consistent with the formation of bonding interactions. A closer analysis suggest that the Ge(1)−Ge(1) (2.733 Å) has a slightly higher ELF value along its bond path, as compared to Ge(2)−Ge(2) (2.766 Å). The −ICOHPs for these two bonds are the same to within two decimal places. Notably, the ELF map also shows a tendency of electron pairing, albeit with lower ELF values, in the center of the triangle. This is a sign of a subtle secondary interaction that also contributes to the stability of the triangle. The secondary interaction appears to be one of the reasons why the intratriangle Ge−Ge bonds are intrinsically stronger than the intertriangle ones (see Table 2). However, the maximum of the ELF in this plane appears as lobes outside the two Ge(1) atoms, which are identified as lone pairs. In the intertriangle region, the Ge(2)−Ge(2) bond (2.635 Å) has a much greater ELF value than the Ge(1)−Ge(1) bonds (2.704 Å) (Figure 6c), revealing a rather general "shorter bonds = stronger bonds" paradigm. In contrast to the triangle of Ge, the triangle composed of the voids in Figure 6c has a low tendency of electron pairing in the center, representing primarily repulsive interactions. The other triangle of Ge (Figure 6d), composed of Ge(4) and Ge(5) atoms, has an almost-symmetric distribution of ELF (for both Ge−Ge bonds and lone pairs). This triangle represents the region of the strongest Ge−Ge bonding in the structure, as clearly revealed in the calculated −ICOHP values. Two adjacent triangular prisms are connected via a single germanium. This linking germanium, Ge(6), illustrated in Figure 5b, is bonded to two atoms comprising a square face in each prism (Ge(1)), and the −ICOHP for each of these bonds is about the same as between germanium atoms comprising two different triangular faces.

Structural Motifs within the Germanium Sublattices at 1 atm. To explore which zero-dimensional motifs may be present in the germanium sublattices, we optimized the geometries of several Ge dimers, trimers, pentamers, and hexamers, varying the charge on the clusters. The bond length calculated for $(Ge_3)^{2-}$, 2.611 Å, is in excellent agreement with the shortest Ge−Ge contact in $P6_3/mmc$-$BaGe_3$. The 2.524 Å bond within the neutral dimer, Ge_2, matches up quite well with distance within the Ge dumbbells in the $I4/mmm$ structure. The trends in bond lengths in a $(Ge_6)^{4-}$ cluster with C_{2v} symmetry (an alternative geometry with D_{3h} symmetry was higher in energy and contained a half-filled HOMO (HOMO = highest occupied molecular orbital) can be compared to those found within this motif in $Amm2$-$BaGe_3$. The Ge−Ge bonds in the triangular faces were calculated as being 2.632 (2.733) Å and 2.977 (2.766) Å, and those in the square faces 2.589 (2.635) Å and 2.746 (2.704) Å for the molecule (and in the solid). $(Ge_6)^{5-}$ and $(Ge_6)^{6-}$ cluster models yielded significantly longer distances, in particular for the Ge(2)−Ge(2) bond, which measures 2.635 Å (2.787 and 2.933 Å for $(Ge_6)^{5-}$ and $(Ge_6)^{6-}$, respectively), giving further support for the $(Ge_6)^{4-}$ assignment.

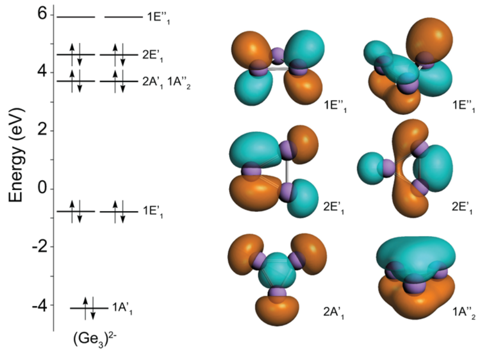

Figure 7. Molecular orbital diagram calculated for a $(Ge_3)^{2-}$ cluster optimized within D_{3h} symmetry. Isosurfaces of orbitals containing Ge $4p$ character (the occupied $2A_1'$, $1A_2''$, $2E_1'$, and unoccupied $1E_1''$ MOs) are illustrated using an isovalue of ±0.03 a.u.

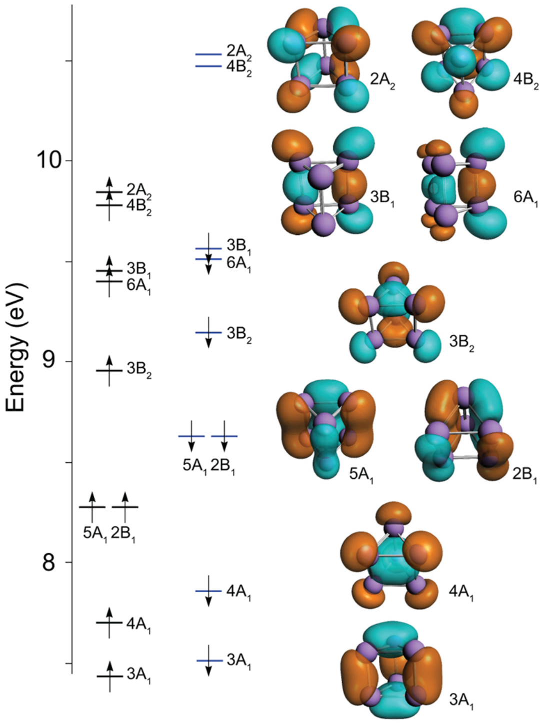

Figure 8. Molecular orbital diagram calculated for a $(Ge_6)^{4-}$ cluster using the geometry extracted from $Amm2$-$BaGe_3$ at 1 atm. Isosurfaces of relevant orbitals of α-spin (the doubly occupied $3A_1$, $4A_1$, $5A_1$, $2B_1$, $3B_2$, $3B_1$, $6A_1$, and singly occupied $2A_2$ and $4B_2$ MOs) are illustrated using an isovalue of ±0.03 a.u.

Since the $(Ge_6)^{4-}$ triangular prism can be understood as two $(Ge_3)^{2-}$ triangles stacked on top of each other, we calculated the MO diagram of the latter; it is illustrated in Figure 7, along with isosurfaces of the important orbitals comprised of linear combinations of the $4p$ orbitals on the Ge atoms. The doubly degenerate $1E_1''$ LUMOs (LUMO = lowest unoccupied molecular orbital) match up with those presented previously for $(Sn_3)^{2-}$.[40] However, whereas Fässler found the $2A_1'$ orbital to be higher in energy than the doubly degenerate $2E_1'$ MOs, we find it to be almost degenerate with the $1A_2''$, which is composed of an in-phase combination of those $4p$ orbitals perpendicular to the triangular plane. Next, we calculated the MOs of a $(Ge_6)^{4-}$ cluster using the germanium coordinates extracted from the extended system. In a restricted calculation, two nearly degenerate orbitals vied to be the HOMO, but the system had only two electrons with which they could be filled. Because of this, unrestricted calculations assuming a triplet electronic configuration were carried out. The molecular orbital diagram is illustrated in Figure 8, along with isosurfaces of the orbitals of α-spin that can be constructed from the MOs of $(Ge_3)^{2-}$ containing Ge $4p$ character (the β-spin orbitals were qualitatively similar). The $3A_1$, $4A_1$, and $5A_1/2B_1$ orbitals of $(Ge_6)^{4-}$ are clearly composed of an in-phase combination of the $1A_2''$, $2A_1'$, and doubly degenerate $2E_1'$ MOs of $(Ge_3)^{2-}$, while the $3B_2$ is an out-of-phase combination of the $2A_1'$. Whereas all of the aforementioned $(Ge_6)^{4-}$ MOs are comprised of MOs that are occupied in $(Ge_3)^{2-}$, the $3B_1$ and $6A_1$ orbitals are different. These are constructed from in-phase combinations of the doubly degenerate LUMOs of the trimer and are $p\sigma$-bonding across the contacts belonging to the square faces. As a result of this favorable bonding interaction, their energy is lowered with respect to combinations of the $2E_1'$ orbitals, which are antibonding between the two triangular faces.

What is the best way to interpret the bonding in the $(Ge_5)^{x-}$ cluster of C_{2v} symmetry that is surrounded by a 2D Ba lattice? Even though anionic isolated clusters do not truly exist within the solid, because of covalent interactions between structural motifs and the presence of excess metallic electrons, it is still instructive to attempt to assign charges to distinct clusters. For example, an ELF analysis led to the conclusion that Eu_3Ge_5 was comprised of $(Ge_5)^{6-}$ clusters whose geometry was distorted from the ideal trigonal bipyramid by the cationic environment, and the ratio of the skeletal and exohedral electrons.[23] Sr_3Sn_5, Ba_3Sn_5, and Ba_3Pb_5 were also found to contain distorted square pyramidal *arachno*-clusters of the Wade-type, $(Pb_5)^{6-}$ and $(Sn_5)^{6-}$.[25] On the other hand, the clusters in Sr_3Sn_5 and La_3Sn_5 have been interpreted as *nido*-Sn_5^{4-} distorted square pyramids,[26] and the electron count in Yb_3Ge_5 has been assigned as $Yb^{2.4+}[Ge_5]^{4-}\cdot 3.2e^-$(with the excess 3.2 electrons being itinerant).[24] Because the −ICOHPs for the contacts linking the $(Ge_6)^{4-}$ and $(Ge_5)^{x-}$ clusters were only 0.32 and 0.49 eV/bond mol, indicating that the bonding between these motifs is relatively weak, we concluded that it is reasonable to approximate them as distinct entities.

Key to understanding $(Ge_5)^{x-}$ is the observation that the bond lengths of the atoms comprising the central trimer, and their −ICOHPs, are in good agreement with those calculated for the $(Ge_3)^{2-}$ unit found in $P6_3/mmc$-$BaGe_3$. Because of this, it is unlikely that the cluster can be classified as a *nido*-$(Ge_5)^{4-}$ or *arachno*-$(Ge_5)^{6-}$ (for which we calculate the Ge(4)−Ge(4) distances to be 3.445 and 3.874 Å, respectively). However, because the −ICOHPs indicate that the bonds between the apical Ge atoms and those within the triangle are just as strong as the bonds between Ge atoms comprising the triangular face in $(Ge_6)^{4-}$, this motif cannot be viewed as two Ge atoms capping a $(Ge_3)^{2-}$ cluster with which they do not interact. This led us to optimize the geometry of a $(Ge_5)^{2-}$ cluster, and the bond lengths of the resulting D_{3h} symmetry cluster were in reasonable agreement with those extracted from the solid (Ge(3)−Ge(4) and Ge(3)−Ge(5): 2.674 Å, Ge(4)−Ge(4) and Ge(5)−Ge(4) 2.909 Å), providing further support for this assignment. Single-point calculations on the unoptimized C_{2v} symmetry $(Ge_5)^{2-}$ cluster yielded the MO diagram in Figure 9. The MOs of $(Ge_5)^{2-}$ can be understood in terms of the MOs of $(Ge_3)^{2-}$ interacting with the 4*p* orbitals of the apical Ge atoms (cf. Figure 9 and Figure 7). For example, the $4A_1$ $(2A_1'' + p_z)$, $2B_2$ $(1A_2'' + p_z)$, $1A_2$ $(1E_1'' + p_x)$, $3B_2$ $(1E_1'' + p_y)$, $5A_1$ $(2E_1' + p_x)$, and $2B_1$ $(2E_1' + p_y)$ MOs of the $(Ge_5)^{2-}$ cluster are comprised of the orbitals of $(Ge_3)^{2-}$ and the apical germanium orbitals given in the braces. The Ge(6) atom was assigned a charge of zero, leaving two metallic electrons, under the assumption that the Ba atoms assume a charge of +2. Therefore, the proposed electron count is $4[Ba^{2+}][Ge_6]^{4-}[Ge_5]^{2-}Ge^0\cdot(2.0e^-)$.

Electronic Structure at 1 atm. Figure 10 shows the density of states (DOS) and the projected DOS of the newly predicted *Amm*2 and *I*4/*mmm* structures calculated at atmospheric pressure. Both structures are clearly metallic, as seen from the absence of an energy gap in the DOS. Of particular interest is the fact that the Fermi energy (E_F) in both structures lies on a peak just below the pseudo-gap. This indicates a rather high value of the DOS at the Fermi level, which is required to achieve a non-negligible T_c. The calculated DOS at E_F for the *Amm*2 and *I*4/*mmm* structures are 2.09×10^{-2} and 1.69×10^{-2} eV^{-1} Å^3, respectively; the latter is already close to the value of bulk gold. The DOS near the Fermi level was found to exhibit primarily Ge 4*p* and Ba 5*d* character, implying that full electron donation from the alkaline-earth metal to germanium does not occur. This finding is consistent with Pyykkö's classification of barium as an "honorary *d*-element".[44,45] The low-lying bands between −12 V to −6 eV are primarily composed of Ge 4*s* orbitals. In the *Amm*2 structure, these bands are separated from the valence bands (primarily Ge 4*p* and Ba 5*d* hybridized bands) by a gap of ca. 1.6 eV. In the *I*4/*mmm* structure, however, such a gap is not found. This is indicative of an enhanced orbital overlap in the *I*4/*mmm* structure, which stabilizes the bonding interactions and destabilizes the antibonding interactions and therefore increases the overall bandwidths. It appears that this band expansion in the *I*4/*mmm* structure is associated with a substantially shorter nearest-neighbor Ge−Ge contact (2.517 Å; see Table 2), as compared with that in the *Amm*2 structure (2.635 Å). The same feature has also been found in the DOS of $CaSi_3$ calculated in the *I*4/*mmm* structure.[36]

Superconductivity. To investigate the possibility of phonon-mediated superconductivity in the predicted phases

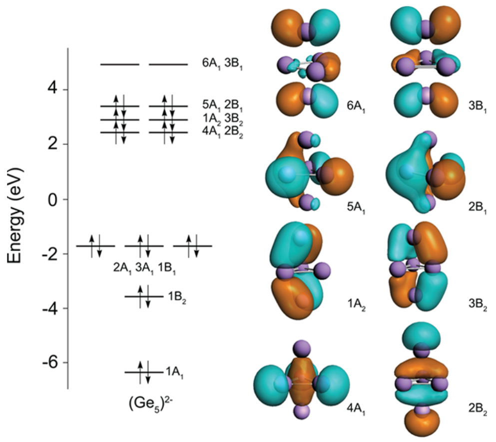

Figure 9. Molecular orbital diagram calculated for a $(Ge_5)^{2-}$ cluster using the geometry extracted from *Amm*2-$BaGe_3$ at 1 atm. Isosurfaces of relevant orbitals (the occupied $5A_1$, $2B_1$, $1A_2$, $3B_2$, $4A_1$, $2B_2$, and unoccupied $6A_1$, $3B_2$ MOs) are illustrated using an isovalue of ±0.025−0.03 a.u.

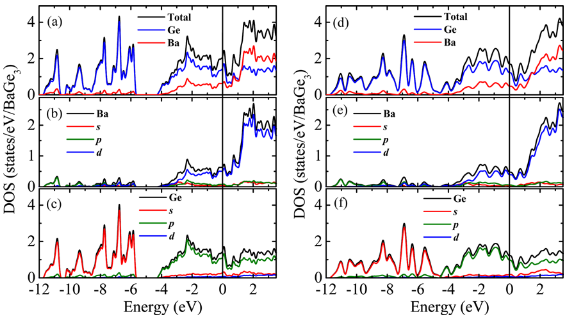

Figure 10. Electronic density of states (DOS) and its projections to elements and orbitals for (a−c) the *Amm*2 structure and (d−f) the *I*4/*mmm* structure.

of $BaGe_3$, the phonon spectral function $\alpha^2F(\omega)$, logarithmic average of the phonon frequencies $\omega_{\log}$, and electron−phonon coupling parameter λ, were calculated as a function of pressure (see Table 3). The superconducting critical temperatures (T_c) for these phases were estimated using the Allen−Dynes modified McMillan formula:[46,47]

$$T_c = \frac{\omega_{\log}}{1.2}\exp\left[\frac{-1.04(1+\lambda)}{\lambda - \mu^*(1.062\lambda)}\right] \tag{1}$$

The calculated T_c values are shown in Figure 11a, as a function of pressure. This methodology was based on an extension of the BCS model to include the explicit forms of the electron−phonon interactions (as opposed to assuming a constant interaction for all modes).[48,49] The average strength of the attractive interactions is characterized by λ, given as

$$\lambda = 2\int_0^{\infty}\frac{\alpha^2F(\omega)}{\omega}\,d\omega \tag{2}$$

incorporating contributions from all participating phonon modes.

Table 3. Electron-Phonon Coupling Parameter (λ), Logarithmic Average of Phonon Frequencies ($\omega_{\log}$), and Estimated Superconducting Critical Temperature (T_c) for Different Phases of $BaGe_3$ Calculated at Selected Pressures

phase	pressure	λ	$\omega_{\log}$ (K)	T_c (K)
$P6_3/mmc$	1 atm	0.73	122.4	4.0
$Amm2$	1 atm	0.86	95.3	4.5
$I4/mmm$	1 atm	0.86	116.2	5.5
$I4/mmm$	25 GPa	0.51	179.7	1.7
$R\bar{3}m$	35 GPa	0.48	209.1	1.4
$P\bar{6}m2$	50 GPa	0.68	133.6	3.6
$P\bar{6}m2$	100 GPa	0.66	134.2	3.2
$P\bar{6}m2$	150 GPa	0.64	138.8	3.0

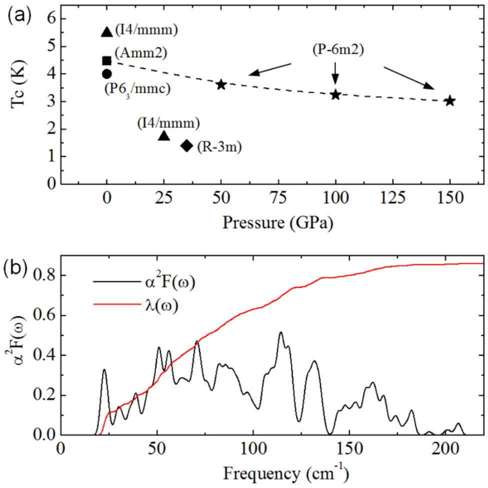

Figure 11. (a) Calculated superconducting critical temperatures (T_c) for different phases of $BaGe_3$. (b) The Eliashberg phonon spectral function, $\alpha^2F(\omega)$, and electron−phonon integral, $\lambda(\omega)$, for the *Amm*2 phase at atmospheric pressure.

The phonon spectral function was calculated by summing over the frequency-weighted phonon line width γ_{qj} for all participating modes (qj) in the first Brillouin zone,

$$\alpha^2F(\omega) = \frac{1}{2\pi N(\varepsilon_F)}\sum_{qj}\frac{\gamma_{qj}}{\omega_{qj}}\delta(\omega - \omega_{qj})w(q) \tag{3}$$

Here, $w(q)$ is the weight of the mode (qj) and $N(\varepsilon_F)$ is the DOS at the Fermi level, The γ_{qj} were calculated as

$$\gamma_{qj} = 2\pi\omega_{qj}\sum_{nm}\int\frac{d^3k}{\Omega_{BZ}}|g^j_{kn,k+qm}|^2\delta(\varepsilon_{kn} - \varepsilon_F)\delta(\varepsilon_{k+qm} - \varepsilon_F) \tag{4}$$

where the integral is taken over the first Brillouin zone. ε_{kn} and ε_{k+qm} are the Kohn−Sham eigenvalues with wave vectors k and k+q in the n^{th} and m^{th} band. $g^j_{kn,k+qm}$ is the electron−phonon matrix element determined from the linearized self-consistent potential.

The repulsive electron-screened interactions are represented by the Coulomb pseudo-potential μ^*. It is a "pseudo" parameter estimated by rescaling the Coulomb repulsion parameter μ to include retardation effects,

$$\mu^* = \frac{\mu}{1 + \mu\ln(T_F/\Theta_D)} \tag{5}$$

where T_F and Θ_D are the Fermi and Debye temperatures. Since the numerical evaluation of μ^* is difficult, empirical values are often used. For typical metals, empirical values of μ^* between 0.1 and 0.13 are generally considered to be reasonable.[50] In the present study, we determined the μ^* value for $BaGe_3$ to be 0.122, by fitting the experimentally measured T_c (4 K) of the $P6_3/mmc$ phase to the Allen−Dynes-modified McMillan formula, along with the calculated values of λ and $\omega_{\log}$.

All predicted phases of $BaGe_3$ were suggested to be potentially superconducting; the estimated T_c appears to be sensitive to the choice of structures and varies from 1.4 to 5.5 K at different pressures (Table 3). The superconductivity is attained primarily by the large electron−phonon coupling that compensates for the low phonon frequencies, $\omega_{\log}$, induced by the heavy atomic masses of Ba and Ge. In addition, a considerable density of states for the Ge 4*p* and Ba 5*d* bands at the Fermi level (Figure 10) is also regarded as an advantage to facilitate the formation of Cooper pairs. The calculated λ of the $P6_3/mmc$ structure at ambient pressure is 0.73, which is consistent with the values for YSi_3 (0.6) and $LuSi_3$ (0.65).[36] The *Amm*2 and *I*4/*mmm* structures have a greater λ (0.86) and, therefore, are predicted to have a slightly higher T_c. For comparison purposes, the calculated value of λ for Sn, which is a typical BCS superconductor at ambient pressure, is 0.46 at the same level of theory.[51] The phonon spectral function, $\alpha^2F(\omega)$, and the integrated $\lambda(\omega)$ for the *Amm*2 structure is presented in Figure 11b. Clearly the phonon modes at different frequency regions contribute almost uniformly to the λ, signifying an isotropic electron−phonon coupling. This is in contrast to the electron−phonon coupling in the extended structures of strong anisotropic nature, e.g., MgB_2, where the electron−phonon interaction has a large variation in its strength at different phonon modes.[52] The calculated T_c for the *I*4/*mmm* structure is 5.5 K. In comparison, the measured T_c in the isostructural $CaSi_3$, YSi_3, $CaGe_3$, and $LuSi_3$, are 4.0, 5.0, 6.8, and 7.1 K, respectively.[35,36] This indicates that the T_c of this structure family is tunable to some extent through the choice of constituent elements, by virtue of tailoring the metal-network interactions and modifying the DOS at the Fermi level.

CONCLUSIONS

Evolutionary structure searches coupled with structural analogies were carried out to predict novel $BaGe_3$ structures at pressures up to 250 GPa, and three hitherto unsynthesized phases were found. $I4/mmm$-$BaGe_3$ is isotypic with a previously synthesized $CaGe_3$ structure[35] that has since been attained in $CaSi_3$, YSi_3, and $LuSi_3$.[36] It is thermodynamically and dynamically stable between 15.6 GPa and 35.4 GPa, and remains dynamically stable down to 1 atm. Above 35.4 GPa two isoenthalpic phases of $P\bar{6}m2$ and $R\bar{3}m$ symmetry become stable, and they remain the global minima to the highest pressures considered. Their structures consisted of layers of unique double Kagome nets comprised of Ge atoms, separated by Ba−Ge layers in which the Ge atoms assume a diamondoid framework that encompasses corner-sharing Ge clusters. The $R\bar{3}m$ structure was not dynamically stable at 1 atm, but upon decompression $P\bar{6}m2$-$BaGe_3$ transformed to the dynamically stable $Amm2$ structure. These results suggest that high-pressure high-temperature synthesis techniques could potentially be used to synthesize two new $BaGe_3$ phases with $I4/mmm$ and $Amm2$ symmetry. The 1 atm $Amm2$ structure could be interpreted as containing four Ba^{2+} cations, $[Ge_6]^{4-}$ and $[Ge_5]^{2-}$ clusters, along with neutral Ge atoms linking two $[Ge_6]^{4-}$ triangular prisms and two itinerant electrons per primitive unit cell. The Allen−Dynes-modified McMillan formula was employed to estimate the T_c of the $BaGe_3$ structures, as a function of pressure. The superconducting transition temperature increases slightly with decreasing pressure, and at 1 atm, the T_c values of the newly predicted $I4/mmm$ (5.5 K) and $Amm2$ (4.5 K) phases are comparable to that of the known $P6_3/mmc$ phase (4 K).[33]

COMPUTATIONAL DETAILS

Evolutionary algorithm (EA) structure searches on the $BaGe_3$ stoichiometry were carried out using Release 8 of XtalOpt[37,53] on structures containing 2, 3, 4, and 6 formula units in the primitive cell at 0, 25, 50, 150, and 250 GPa. Exploratory calculations at 50 and 150 GPa, with five formula units, revealed that the enthalpies of the most stable structures located were significantly higher than the global energy minima. This suggests that phases constructed from the Ba_5Ge_{15} repeat unit are not thermodynamically stable, so evolutionary searches for this cell size were not performed at any other pressure. In order to accelerate the Ba_6Ge_{18} runs, they were seeded with supercells of the most stable structures obtained for Ba_2Ge_6 and Ba_3Ge_9, as well as particularly stable and unique Ba_6Ge_{18} phases found at other pressures. Duplicates were detected during the EA run using the XtalComp algorithm.[42] In addition to the EA runs, calculations were carried out on the $I4/mmm$ structure that was experimentally observed for $CaGe_3$,[35] as well as MSi_3 (M = Ca, Y, Lu).[36] The $BaPb_3$ ($R\bar{3}m$)[54] and $CaSn_3$[55] structures were also considered, but their enthalpies were not competitive with the most stable phases. For each stoichiometry, a subset of the geometries with the lowest enthalpy were relaxed in the pressure range of 0−250 GPa.

Geometry optimizations and electronic structure calculations were performed using density functional theory (DFT), as implemented in the Vienna *ab initio* Simulation Package (VASP) versions 4.6.31 and 5.2.12.[56] The projector augmented wave (PAW) method[57] was used. For the structure searches the Ba 5*s*/5*p*/6*s* electrons were treated explicitly, and the standard Ge PAW potential was employed, along with an energy cutoff of 280 eV. For the enthalpy calculations, the same Ba 5*s*/5*p*/6*s* potential was employed, but the Ge 3*d*/4*s*/4*p* electrons were considered and the energy cutoff was increased to 540 eV. The gradient corrected exchange and correlation functional of Perdew−Burke−Ernzerhof (PBE)[58] was adopted, and the *k*-point grids were generated using the Γ-centered Monkhorst−Pack scheme. The number of divisions along each reciprocal lattice vector was chosen such that the product of this number with the real lattice constant was 25 Å in the structural searches. In the enthalpy calculations, dense *k*-point grids were selected to yield total energies that were converged to within 0.5 meV/atom for each structure.

Phonon calculations for the predicted structures of $BaGe_3$ were performed using the Quantum ESPRESSO program[59] employing the linear response method and Trouiller-Martins-type pseudopotentials[60] with the PBE functional and an energy cutoff of 80 Ry. The phonon results were crossed checked with those obtained using VASP and the finite displacement method, and with the ABINIT program[61] using a linear response method. A 4 × 4 × 4 *q*-point mesh and an 8 × 8 × 8 *k*-point mesh were used for the phonon calculations of the $Amm2$, $I4/mmm$, $P\bar{6}m2$, and $R\bar{3}m$ structures. For the $P6_3/mmc$ structure, a 4 × 4 × 6 *q*-point mesh and an 8 × 8 × 12 *k*-point mesh was used. The Quantum ESPRESSO program and the same pseudopotentials were also employed for the electron−phonon coupling (EPC) calculations, which were carried out on the *q*-point meshes listed above. Individual EPC matrices were obtained with a 16 × 16 × 24 *k*-point mesh for the $P6_3/mmc$ structure and a 16 × 16 × 16 *k*-point mesh for the other structures.

The DOS, band structures, COHPs, and −ICOHPs of the $P6_3/mmc$, $I4/mmm$ and $Amm2$ structures at 1 atm were calculated using the tight−binding linear muffin−tin orbital (TB−LMTO) method.[62,63] The VWN[64] local exchange correlation potential was used along with the Perdew−Wang[65] generalized gradient approximation, and scalar relativistic effects were included. The structural parameters were taken from those optimized with VASP, and the DOS agreed well with those calculated using plane waves.

The molecular calculations on the $(Ge_n)^{x-}$ (n = 2, 3, 5, 6) clusters were carried out using the Amsterdam Density Functional (ADF) software package[66,67] and the revPBE generalized gradient density functional.[58] The basis functions on all of the atoms consisted of a triple-ζ Slater-type basis set with polarization functions (TZP) from the ADF basis-set library. The core shells up to 3*d* for Ge were kept frozen.

ASSOCIATED CONTENT

Supporting Information

Structural parameters are given as Supporting Information. This material is available free of charge via the Internet at http://pubs.acs.org.

AUTHOR INFORMATION

Corresponding Authors

*E-mail: ezurek@buffalo.edu (E. Zurek).
*E-mail: yansun.yao@usask.ca (Y. Yao).

Notes

The authors declare no competing financial interest.

ACKNOWLEDGMENTS

We acknowledge the National Science Foundation (NSF) (No. DMR-1005413) and the Natural Sciences and Engineering Research Council of Canada (NSERC) for financial support. E.Z. thanks the Alfred P. Sloan Foundation for a Research Fellowship (2013−2015). The Center for Computational Research at SUNY Buffalo and the Information and Communications Technology group at the University of Saskatchewan are acknowledged for computational support. Part of the calculations were performed by the use of computing resources provided by WestGrid and Compute Canada.

REFERENCES

(1) Menoni, C. S.; Hu, J. Z.; Spain, I. L. *Phys. Rev. B* **1986**, *34*, 362−368.

(2) Nelmes, R. J.; Liu, H.; Belmonte, S. A.; Loveday, J. S.; McMahon, M. I.; Allan, D. R.; Häusermann, D.; Hanfland, M. *Phys. Rev. B* **1996**, *53*, R2907−R2909.

(3) Vohra, Y. K.; Brister, K. E.; Desgreniers, S.; Ruoff, A. L.; Chang, K. J.; Cohen, M. L. *Phys. Rev. Lett.* **1986**, *56*, 1944−1947.

(4) Takemura, K.; Schwarz, U.; Syassen, K.; Hanfland, M.; Christensen, N. E.; Novikov, D. L.; Loa, I. *Phys. Rev. B* **2000**, *62*, R10603−R10606.

(5) Buckel, W.; Wittig, J. *Phys. Lett.* **1965**, *17*, 187−188.

(6) Guloy, A. M.; Ramlau, R.; Tang, Z.; Schnelle, W.; Baitinger, M.; Grin, Y. *Nature* **2006**, *443*, 320−323.

(7) Cui, H. B.; Graf, D.; Brooks, J. S.; Kobayashi, H. *Phys. Rev. Lett.* **2009**, *102*, 237001-1−237001-4.

(8) Bundy, F. P.; Kasper, J. S. *Science* **1963**, *139*, 340−341.

(9) Nelmes, R. J.; McMahon, M. I.; Wright, N. G.; Allan, D. R.; Loveday, J. S. *Phys. Rev. B* **1993**, *48*, R9883−R9886.

(10) Johnson, B. C.; Haberl, B.; Deshmukh, S.; Malone, B. D.; Cohen, M. L.; McCallum, J. C.; Williams, J. S.; Bradby, J. E. *Phys. Rev. Lett.* **2013**, *110*, 085502-1−0855-2-5.

(11) Schwarz, U.; Wosylus, A.; Böhme, B.; Baitinger, M.; Hanfland, M.; Grin, Y. *Angew. Chem., Int. Ed.* **2008**, *47*, 6790−6793.

(12) Selli, D.; Baburin, I. A.; Martoňak, R.; Leoni, S. *Sci. Rep.* **2013**, *3*, 1466-1−1466-6.

(13) Chen, X.-J.; Zhang, C.; Meng, Y.; Zhang, R.-Q.; Lin, H.-Q.; Struzhkin, V. V.; Mao, H.-K. *Phys. Rev. Lett.* **2011**, *106*, 135502-1−135502-4.

(14) Bobev, S.; You, T.-S.; Suen, N.-T.; Saha, S.; Greene, R.; Paglione, J. *Inorg. Chem.* **2012**, *51*, 620−628.

(15) Bobev, S.; Bauer, E. D.; Thompson, J. D.; Sarrao, J. L.; Miller, G. J.; Eck, B.; Dronskowski, R. *J. Solid State Chem.* **2004**, *177*, 3545−3552.

(16) Evers, J.; Oehlinger, G.; Weiss, A. *J. Less-Common Met.* **1980**, *69*, 399−402.

(17) Fukuoka, H.; Yamanaka, S.; Matsuoka, E.; Takabatake, T. *Inorg. Chem.* **2005**, *44*, 1460−1465.

(18) Suen, N. T.; Hooper, J.; Zurek, E.; Bobev, S. *J. Am. Chem. Soc.* **2012**, *134*, 12708−12716.

(19) Siggelkow, L.; Hlukhyy, V.; Fässler, T. F. *J. Solid-State Chem.* **2012**, *191*, 76−89.

(20) Fukuoka, S.; Yoshikawa, H.; Baba, M.; Yamanaka, K. *Bull. Chem. Soc. Jpn.* **2010**, *83*, 323−327.

(21) Scharfe, S.; Fässler, T. F. *Philos. Trans. R. Soc. A* **2010**, *368*, 1265−1284.

(22) Scharfe, S.; Kraus, F.; Stegmaier, S.; Schier, A.; Fässler, T. F. *Angew. Chem., Int. Ed.* **2011**, *50*, 3630−3670.

(23) Budnyk, S.; Weitzer, F.; Kubata, C.; Prots, Y.; Akselrud, L. G.; Schnelle, W.; Hiebl, K.; Nesper, R.; Wagner, F. R.; Grin, Y. *J. Solid-State Chem.* **2006**, *179*, 2329−2338.

(24) Harada, M.; Fukuoka, H.; Matsumura, D.; Inumaru, K. *J. Phys. Chem. C* **2012**, *116*, 2153−2158.

(25) Zürcher, F.; Nesper, R.; Hoffmann, S.; Fässler, T. F. *Z. Anorg. Allg. Chem.* **2001**, *627*, 2211−2219.

(26) Klem, M. T.; Vaughey, J. T.; Harp, J. G.; Corbett, J. D. *Inorg. Chem.* **2001**, *40*, 7020−7026.

(27) Kauzlarich, S. M., Ed. *Chemistry, Structure and Bonding of Zintl Phases and Ions*; VCH Publishers: New York, 1996.

(28) Albert, K.; Meyer, H.-J.; Hoffmann, R. *J. Solid-State Chem.* **1993**, *106*, 201−210.

(29) Fukuoka, H.; Baba, K.; Yoshikawa, M.; Ohtsu, F.; Yamanaka, S. *J. Solid-State Chem.* **2009**, *182*, 2024−2029.

(30) Fukuoka, H.; Yamanaka, S. *Phys. Rev. B* **2003**, *67*, 094501-1−094501-5.

(31) Akselrud, L.; Wosylus, A.; Castillo, R.; Aydemir, U.; Prots, Y.; Schnelle, W.; Grin, Y.; Schwarz, U. *Inorg. Chem.* **2014**, *53*, 12699−12705.

(32) Castillo, R.; Carrillo-Cabrera, W.; Schwarz, U.; Grin, Y. *Inorg. Chem.* **2015**, *54*, 1019−1025.

(33) Fukuoka, H.; Tomomitsu, Y.; Inumaru, K. *Inorg. Chem.* **2011**, *50*, 6372−6377.

(34) Fukuoka, H.; Suekuni, K.; Onimaru, T.; Inumaru, K. *Inorg. Chem.* **2011**, *50*, 3901−3906.

(35) Schnelle, W.; Ormeci, A.; Wosylus, A.; Meier, K.; Grin, Y.; Schwarz, U. *Inorg. Chem.* **2012**, *51*, 5509−5511.

(36) Schwarz, U.; Wosylus, A.; Rosner, H.; Schnelle, W.; Ormeci, A.; Meier, K.; Baranov, A.; Nicklas, M.; Leipe, S.; Müller, C. J.; Grin, Y. *J. Am. Chem. Soc.* **2012**, *134*, 13558−13561.

(37) Lonie, D. C.; Zurek, E. *Comput. Phys. Commun.* **2011**, *182*, 372−387.

(38) Katzke, H.; Tolédano, P. *Phys. Rev. B* **2007**, *75*, 174103-1−174103-10.

(39) Katzke, H.; Bismayer, U.; Tolédano, P. *Phys. Rev. B* **2006**, *73*, 134105-1−134105-10.

(40) Fässler, T. F.; Kronseder, C. *Angew. Chem., Int. Ed. Engl.* **1997**, *36*, 2683−2686.

(41) Zurek, E.; Grochala, W. *Phys. Chem. Chem. Phys.* **2015**, *17*, 2917−2934.

(42) Lonie, D. C.; Zurek, E. *Comput. Phys. Commun.* **2012**, *183*, 690−697.

(43) Gao, G.; Ashcroft, N. W.; Miao, M.; Hoffmann, R. *J. Phys. Chem. C* **2014**, *118*, 25167−25175.

(44) Gagliardi, L.; Pyykkö, P. *Theor. Chem. Acc.* **2003**, *110*, 205−210.

(45) Zurek, E.; Autschbach, J.; Malinowski, N.; Enders, A.; Kern, K. *ACS Nano* **2008**, *2*, 1000−1014.

(46) McMillan, W. L. *Phys. Rev.* **1968**, *167*, 331−344.

(47) Allen, P. B.; Dynes, R. C. *Phys. Rev. B* **1975**, *12*, 905−922.

(48) Eliashberg, G. M. *Zh. Eksp. Teor. Fiz.* **1960**, *38*, 966−976.

(49) Yao, Y.; Tse, J. S.; Tanaka, K.; Marsiglio, F.; Ma, Y. *Phys. Rev. B* **2009**, *79*, 054524 (1−11).

(50) Ashcroft, N. W. *Phys. Rev. Lett.* **2004**, *92*, 187002 (1−4).

(51) Chang, K. J.; Cohen, M. L. *Phys. Rev. B* **1986**, *34*, 4552−4557.

(52) Liu, A. Y.; Mazin, I. I.; Kortus, J. *Phys. Rev. Lett.* **2001**, *87*, 087005 (1−4).

(53) Lonie, D. C.; Zurek, E. *Comput. Phys. Commun.* **2011**, *182*, 2305−2306.

(54) Sands, D. E.; Wood, D. H.; Ramsey, W. J. *Acta Crystallogr.* **1964**, *17*, 986−989.

(55) Wendorff, M.; Röhr, C. *Z. Anorg. Allg. Chem.* **2011**, *637*, 1013−1023.

(56) Kresse, G.; Hafner, J. *Phys. Rev. B* **1993**, *47*, R558−R561.

(57) Blöchl, P. E. *Phys. Rev. B* **1994**, *50*, 17953−17979.

(58) Perdew, J. P.; Burke, K.; Ernzerhof, M. *Phys. Rev. Lett.* **1996**, *77*, 3865−3868.

(59) Giannozzi, P.; et al. *J. Phys.: Condens. Matter* **2009**, *21*, 395502 (1−19).

(60) Troullier, N.; Martins, J. L. *Phys. Rev. B* **1991**, *43*, 1993−2006.

(61) Gonze, X.; et al. *Comput. Phys. Commun.* **2009**, *180*, 2582−2615.

(62) Andersen, O. K. *Phys. Rev. B* **1975**, *12*, 3060−3083.

(63) Andersen, O. K.; Jepsen, O. *Phys. Rev. Lett.* **1984**, *53*, 2571−2574.

(64) Vosko, S. H.; Wilk, L.; Nusair, M. *Can. J. Phys.* **1980**, *58*, 1200−1211.

(65) Perdew, J. P.; Yue, W. *Phys. Rev. B* **1986**, *33*, R8800−R8802.

(66) te Velde, G.; Bickelhaupt, F. M.; Baerends, E. J.; Fonseca Guerra, C.; van Gisbergen, S. J. A.; Snijders, J. G.; Ziegler, T. *J. Comput. Chem.* **2001**, *22*, 931−967.

(67) Baerends, E. J.; Autschbach, J.; Bérces, A.; Bickelhaupt, F. M.; Bo, C.; Boerrigter, P. M.; Cavallo, L.; Chong, D. P.; Deng, L.; Dickson, R. M.; et al.. *ADF2010.01*; http://www.scm.com.